



# Speed independent road classification strategy based on vehicle response: Theory and experimental validation



Yechen Qin<sup>a</sup>, Zhenfeng Wang<sup>a</sup>, Changle Xiang<sup>a</sup>, Ehsan Hashemi<sup>b</sup>, Amir Khajepour<sup>b</sup>, Yanjun Huang<sup>b,\*</sup>

<sup>a</sup> School of Mechanical Engineering, Beijing Institute of Technology, Beijing, People's Republic of China

<sup>b</sup> Mechanical and Mechatronics Engineering Department, University of Waterloo, Waterloo, ON, Canada

## ARTICLE INFO

### Article history:

Received 5 January 2018

Received in revised form 9 June 2018

Accepted 21 July 2018

### Keywords:

Road classification

Frequency domain classifier

Vehicle system responses

Road estimation

## ABSTRACT

This paper presents a speed-independent road classification strategy (SIRCS) based on sole measurement of unsprung mass acceleration. The new method provides an easy yet accurate classification methodology. To this purpose, a classification framework with two phases named off-line and online is proposed. In the off-line phase, the transfer function from unsprung mass acceleration to the road excitation is firstly formulated, and a random forest-based frequency domain classifier is then generated according to the standard road definition of ISO 8608. In the online phase, unsprung mass acceleration and vehicle velocity are firstly combined to calculate the equivalent road profile in the spatial domain, and then a two-step road classifier attributes the road excitation to a certain level based on the power spectral density (PSD) of the equivalent road profile. Simulations are carried out for different classification intervals, varying velocity, system uncertainties and measurement noises. Road experiments are finally performed in a production vehicle to validate the proposed SIRCS. Measurement of only unsprung mass acceleration to identify road classification and less rely on the training data are the major contributions of the proposed strategy.

© 2018 Elsevier Ltd. All rights reserved.

## 1. Introduction

Road condition identification attracts much attention of vehicle manufacturers and government because of vehicle safety and comfort [1,2]. In America, about a quarter of major urban roads are in poor conditions, resulting in extra vehicle maintenance cost of nearly four hundred dollars per driver per year [3]. A report in 2013 revealed that annual road maintenance expenditure was about 20,000 million Euros in EU [4], and roads with poor conditions decrease passengers' feeling and increase travel times [5]. Better road condition information can not only help drivers and advanced vehicle control systems [6–9], but also assist in a better road maintenance scheduling.

Generally speaking, reported road estimation algorithms could be divided into three distinct types, i.e. contact measurement, non-contact measurement and system response based estimation [10]. The first type requires specially designed profilometer, which restricts its commercial application [11]. For the second method, Mono/Stereo cameras and LiDAR are applicable thanks to the vigorous development of autonomous vehicles. Although accurate estimation can be obtained with the non-contact measurement method, high cost of the instruments impedes its application in middle- to low-end vehicles.

\* Corresponding author.

E-mail address: [huangyanjun404@gmail.com](mailto:huangyanjun404@gmail.com) (Y. Huang).

As a result, the third type becomes more and more popular with the help of sensors installed for advanced vehicle dynamics control in mass-produced vehicles [12].

To date, various algorithms have been developed and introduced to the system response based method, which can be classified into two categories from the perspective of model formulation, namely data-driven and model based [13]. Data-driven method formulates black-box model/classifier based on the training data. Ward et al. used a well-trained support vector machine (SVM) classifier to classify real-world road types [14]. Qin et al. used adaptive neuro-fuzzy inference system (ANFIS) [12] and deep neural network (DNN) [15] for road classification and pointed out the unsprung mass is the most suitable system response because of its merits of measurable and relative high classification accuracy [16]. Although data-driven methodology can obtain satisfactory classification result, it still heavily relies on the training data and the accurate extrapolation can not be guaranteed [17]. Model based strategy thus attracts more attention in recent years, where system observer technique is one important component [18–20]. Rath et al. realized the simultaneous estimation of road profile and tire-road friction with a combined higher-order sliding mode and nonlinear Lipschitz observer [21]. Martinez et al. presented an adaptive observer based on Q-parameterizations for semi-active suspension system, which was also experimentally validated. Several attempts have also been made to reconstruct road profile with Kalman-based observer [22,23]. All the studies related to system observer reviewed so far, however, suffer from one common drawback that not all required response information is measurable. Transfer function based road estimation methodology thus emerges as an alternative. Gonzalez et al. used the transfer function from unsprung mass acceleration to road profile to estimate road power spectral density (PSD) [24]. Ward et al. and Wang et al. further extended this approach to varying velocity scenario and performed experiment validation [14,25].

Since no detailed classification algorithm is proposed in [24], and both [14,25] require extensive training data prior to the classification which is impractical for mass-produced vehicles, this paper presents a general framework for road classification without prior training process and independent from the vehicle velocity. The proposed framework contains both online and off-line phases. In the off-line phase, both the inverse transfer function model and the well-trained road class classifier are obtained and stored for online application. As for the online phase, the equivalent road profile in the spatial domain is calculated based on unsprung mass acceleration and vehicle speed. Comprehensive analysis for different driving scenarios and road conditions are numerically investigated, and experimental studies have been conducted to validate the proposed method. The contributions of this paper are:

- A general road classification framework is proposed, which is robust to vehicle velocity and does not rely on extensive training data.
- The SIRCS is robust to system uncertainties and measurement noises. Methods to further improve classification accuracy in noisy environments are also discussed.
- Road tests for different scenarios on various road conditions are performed to validate the algorithm.

The rest of this paper is organized as follows. Section 2 introduces models of road profile and a quarter vehicle; Section 3 presents the classification algorithm and numerical simulation; Section 4 details road experiments; and Section 5 concludes the paper.

## 2. System modeling

This section presents a quarter vehicle transfer function, and details definition of various road levels.

### 2.1. Vehicle transfer function for road classification

This paper uses the transfer function of a quarter vehicle suspension system to formulate the proposed SIRCS. Despite its simplicity, both simulation and field test results show the quarter vehicle model has good accuracy for the presented algorithm. Fig. 1 depicts the structure of quarter vehicle model with the following dynamics:

$$\begin{aligned} m_b \ddot{x}_b + k_s(x_b - x_w) + c_p(\dot{x}_b - \dot{x}_w) &= 0 \\ m_w \ddot{x}_w + k_t(x_w - x_r) + k_s(x_w - x_b) + c_p(\dot{x}_w - \dot{x}_b) &= 0 \end{aligned} \quad (1)$$

where  $m_b$  and  $m_w$  are sprung and unsprung mass;  $k_s$  and  $k_t$  denote the spring and tire stiffness;  $c_p$  represents the damper coefficient, and  $x_b$ ,  $x_w$  and  $x_r$  stand for displacements of the sprung mass, unsprung mass, and road profile, respectively. Note that the tire is simplified to be a spring with only vertical stiffness. The reasons for such simplification are twofold:

- The tire is a complex system containing nonlinearity, time-delay, hysteresis, and uncertainty. Its dynamics have attracted the attention of both academia and the automobile industry, and much remarkable researches have been done on this topic in recent decades [26], however, an accurate tire dynamic model is always unavailable in a real-world application. A simplified tire model is thus necessary for vehicle dynamics analysis.

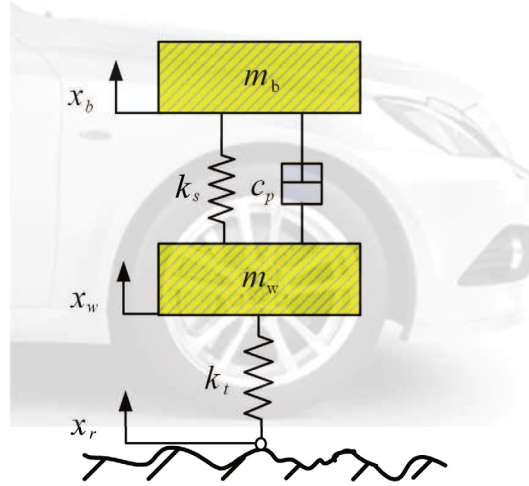


Fig. 1. Structure of quarter vehicle model.

- The primary purpose of this paper is to provide an easy yet accurate road classification methodology based on vehicle vertical response. For the purpose of vertical dynamics analysis, vehicle tire is commonly modeled as a combination of spring and damper [27], that the damper is always neglected [28]. Besides, the proposed algorithm uses a transfer function from the unsprung mass acceleration to road profile to classify the unknown road input; this can be interpreted as a linear approximation of the complex tire dynamic model.

With system parameters shown in Table 1, the transfer function from the unsprung mass acceleration to road profile input can be formulated as in Eq. (2). Previous research [15] showed that of the three measurable vehicle vertical responses, i.e. sprung mass acceleration, unsprung mass acceleration, and rattle space, the unsprung mass acceleration is the most suitable response due to fast convergence and high accuracy, and such observation was also validated on a high-fidelity CarSim full-vehicle model. This result reveals that single measurement of unsprung mass acceleration is sufficient for road classification if the trade-off between accuracy and complexity is the main concern.

$$H(s) = \frac{m_w m_b s^4 + (c_p m_b + c_p m_w) s^3 + A + B + k_t k_s}{m_b k_t s^4 + c_p k_t s^3 + k_s k_t s^2} \quad (2)$$

$$A = (m_w k_s + m_b k_s + m_b k_t + c_p^2 - c_p^2 m_w / m_b) s^2$$

$$B = (c_p k_t + c_p k_s - c_p k_s m_w / m_b) s$$

Based on the transfer function given by Eq. (2), the road classification algorithm will be further discussed in the next section.

## 2.2. Road model

Road irregularities is a function of the distance between the base plate and road surface, and the measured real road profile may contain transient events like potholes and bumps. Since this paper mainly focuses on road statistical characteristic classification instead of road anomaly detection, the assumptions of homogeneous and Gaussian distribution are adopted in this paper. The PSD of any road roughness can be calculated by:

$$G_q(n) = C_{sp} n^{-W} \quad (3)$$

Table 1  
Vehicle parameters.

Parameter	Value
$m_b$	410 kg
$m_w$	37 kg
$k_s$	42,000 N/m
$k_t$	200,000 N/m
$c_p$	2500 Ns/m

**Table 2**  
Road excitation definition.

No.	Description	$W$	$C_{sp}$
1	Smooth Runway (SR)	3	$4.3 \times 10^{-11}$
2	Smooth Highway (SH)	2.6	$1.9 \times 10^{-8}$
3	ISO Level B (ISO-B)	2	$6.4 \times 10^{-7}$
4	Highway with Gravel (HG)	2.1	$4.4 \times 10^{-6}$
5	ISO Level E (ISO-E)	2	$4.1 \times 10^{-5}$
6	Pasture (PA)	1.6	$3 \times 10^{-4}$

where  $n$  is the spatial frequency in  $m^{-1}$ ;  $C_{sp}$  and  $W$  are two constants standing for the excitation energy and road waviness, respectively. Extensive systematic measurements of road conditions in North America and European regions revealed that road waviness located in a broad interval from 1.5 to 3.5 with a mean value of 2.5 as in [29]. Without loss of generality, this paper selects six representative road levels with different  $C_{sp}$  and  $W$  for SIRCS illustration [16]. Table 2 presents the parameters of these six road levels with related abbreviation [30,31]. For a vehicle driving with speed of  $v$ , the time frequency  $f$  can be transformed from the spatial frequency as per  $f = v \cdot n$ .

With road definition given in Eqs. (3), this paper uses the harmony function superposition to generate the road profile in the time domain [32]:

$$x_r(t) = \sum_{u=1}^U \sqrt{2 \cdot G_q(f_{mid-u}) \cdot \frac{f_2 - f_1}{U}} \sin(2\pi f_{mid-u}t + \Phi_{u-l}) \quad (4)$$

where  $U$  is the total number of the time frequency components;  $f_{mid-u}$  is  $u^{th}$  middle frequency in Hz,  $G_q(f_{mid-u})$  is PSD of  $f_{mid-u}$  in  $m^3$ ,  $\Phi_{u-l}$  is independent and identically distributed (IID) random phase over  $(0, 2\pi)$ .  $f_1$  and  $f_2$  are 0.33 Hz and 28.3 Hz, respectively [31]. Typically, the PSD of any generated road profile is plotted in the log-log diagram. Since the widely adopted constant bandwidth PSD calculation method will result in over-emphasized fluctuations especially in the high frequencies ranges, this paper uses the PSD smoothing method recommended by ISO 8608 and more details can be found in [31].

For a quantitative description of road condition, ISO 8608 defines road levels from level A to level H with different  $C_{sp}$  and constant waviness equals to 2. To facilitate SIRCS formulation, this paper (1) merges two adjacent ISO road levels to form a new road class, i.e., level A and B to “Good”, level C and D to “Average”, level E and F to “Poor” and level G and H to “Very poor”; (2) decides the class depending on the bounds of center frequencies from 0.0625 to 2 (cycles/m) [31]. The graphic representation of aforementioned road definition is presented in Fig. 2. Fig. 2(a) depicts the relationships among ISO road levels, merged road classes and representative road levels are given in Table 2. It can be seen that SR, SH and ISO-B locate in “Good” class, HG belongs to “Average” class, and “Bad” class includes both ISO-E and PA. All these six representative road levels cover the waviness range from 1.6 to 3 and the whole road spatial space up to ISO-F, and the comprehensiveness of the representative road levels can thus be ensured. As for Fig. 2(b), the originally generated, the smoothed ISO-B level along with ISO level bounds are depicted as an example. The six center frequencies on 0.0625, 0.125, 0.25, 0.5, 1, and 2 and their boundaries will be used for road classification in the next section.

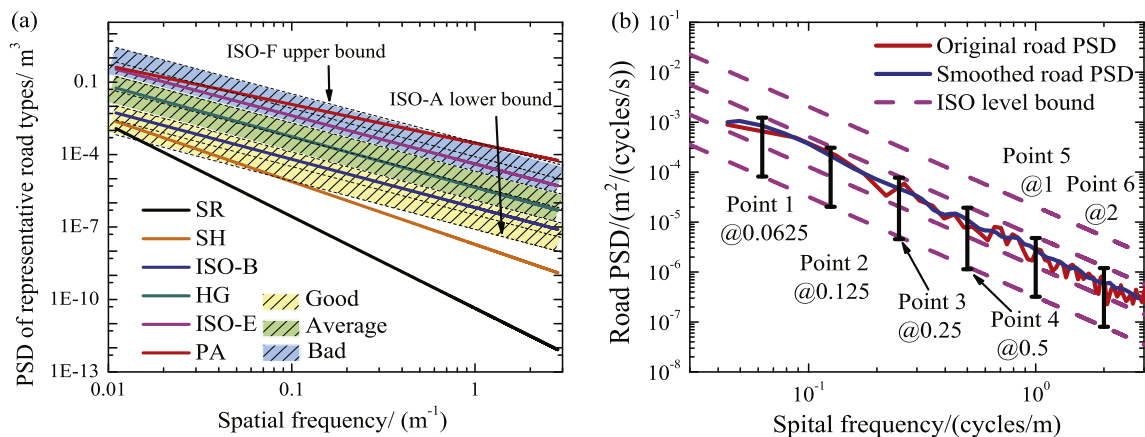


**Fig. 2.** Road definition: (a) Road classes and representative levels, (b) Smoothing and level decision.

### 3. Classification algorithm and simulation results

This section firstly describes the proposed classification algorithm, and then presents the numerical simulation results for different classification interval, varying vehicle speed, the presence of model uncertainties, and noisy environments to show its superiorities.

#### 3.1. Overall structure of SIRCS

The main purpose of the proposed SIRCS is to attribute any unknown road input into the six representative road levels given in Table 2 regardless of vehicle speed. To this end, Fig. 3 shows the overall structure of SIRCS. The proposed SIRCS contains two phases, namely off-line phase and online. The output of off-line phase is twofold: (1) system transfer function from vehicle suspension model, (2) random forest based frequency domain classifier generate according to ISO 8608. In the online phase, vehicle unsprung mass acceleration  $\ddot{x}_w$  is firstly sampled, and then the equivalent road profile  $x_r(t)$  is generated via transfer function in Eq. (2), and the equivalent road profile refer to the estimated road in the time domain. Although it is not exactly the same with the actual excitation at each time sample, the equivalent road profile can still be considered containing similar statistical characteristics with the actual road input. With vehicle velocity measurement  $v(t)$ ,  $x_r(t)$  is then transformed to be road profile in the spatial domain, i.e.,  $x_r(x)$ . Note that vehicle speed  $v(t)$  can be measured by GPS or estimated by kinematic or tire model-based observers [33–37]. A corner-based time-varying velocity estimator robust to road friction changes and power transmission configurations is developed and experimentally tested in [33,36] by combining kinematic and model-based approaches. A fault-tolerant opinion dynamics approach is developed and experimentally verified in [34] to enhance the reliability of the vehicle velocity estimator and to increase robustness to model uncertainties, disturbances, and time delay via solving a convex optimization problem. The signal processing procedure including band pass filtering, framing, PSD calculation, and smoothing are subsequently performed to obtain the smoothed PSD [16]. Random forest-based frequency domain classifier and detailed road level categorizer form the overall road classifier, and use the PSD to attribute road excitation into a level with the highest possibility.

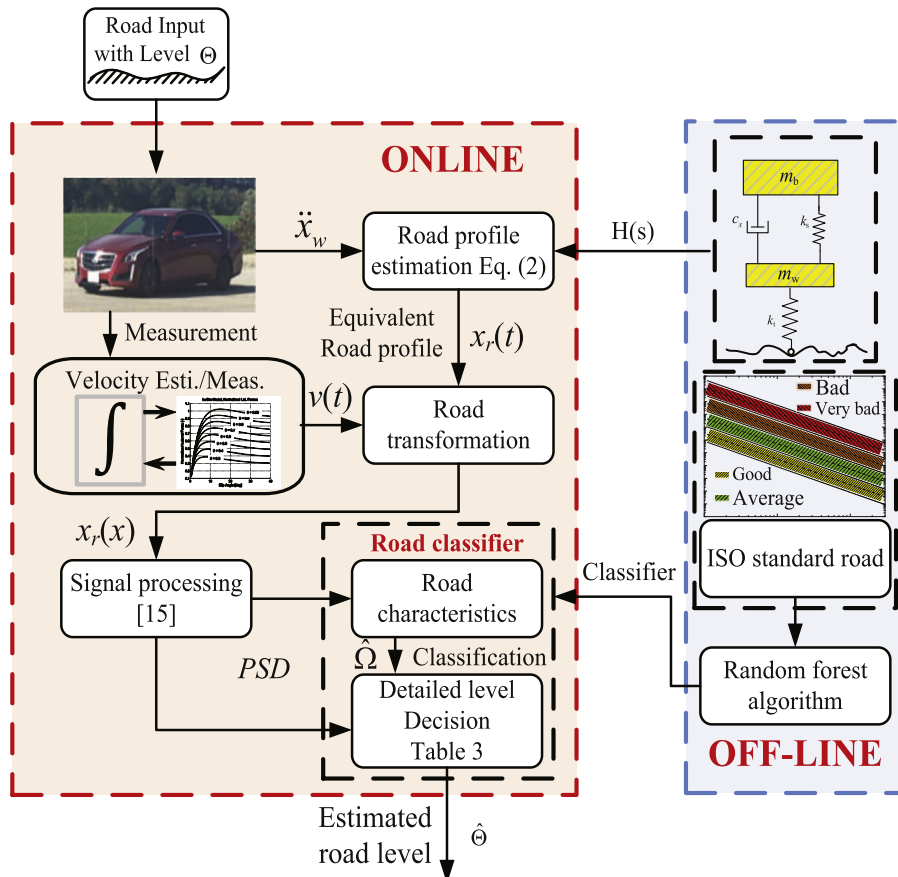


Fig. 3. Overall structure.

### 3.2. Two-step road classifier formulation

To attribute road input into a certain level, this paper uses a two-step classifier in the online phase. The first one utilizes the random forest-based frequency domain classifier to generate a rough road class, and then a detailed level decision procedure is performed to determine the level of road excitation.

#### (1) Random forest-based frequency domain classifier

As shown in Fig. 2(b), ISO 8608 defines both upper and lower bounds of each ISO standard level at different center frequencies. In this case, we use a random forest-based frequency domain classifier to determine a rough excitation road class  $\hat{\Omega}$ . Random forest is composed of numerous decision trees generated by independently sampled random vector from the system input space [38]. The well-trained random forest classifier can sort the input into the class with the highest possibility based on the Gini index:

$$\sum_{al \neq bl} (f(C_{bl}, T)/|T|)(f(C_{al}, T)/|T|) \quad (5)$$

where  $T$  is the training set, and  $f(C_{bl}, T)/|T|$  is the possibility that the selected input belongs to a class  $C_{bl}$ . In this paper, classifier inputs are PSD values at six center frequencies, and output is one of the four road classes, i.e., Good, Average, Poor and Very poor. Note that the random forest based classifier is only for procedure illustration here and numerous of other classify algorithms can be used as well, e.g., adaptive neural fuzzy inference system (ANFIS) [12] and deep neural network (DNN) [15].

#### (2) Detailed road level decision procedure

When the road class is classified, a level decision procedure shown in Table 3 is subsequently performed to determine the detailed road level  $\hat{\Theta}$ . The critical parameter for detailed level decision is the estimated waviness  $\hat{W}$ , which is the linear fitting result in the log–log space according to the smoothed PSD. The boundary conditions shown in Table 3 are determined based on the road definitions given in Table 2. Since there is no road information prior to vehicle traveling, all road levels shown in Table 2 are equally weighted in the proposed algorithm. To be specific, taken road class ‘Bad’ as an example, the boundary value 1.8 is the mean value of road waviness  $W$  for both ISO-E and PA.

Based on the aforementioned two-step classifier, road excitation can now be classified to one certain level with only unsprung mass acceleration measurement. To further illustrate this process, one example ISO-B road is generated for the length of 400 m with a velocity of 36 km/h as per Eq. (4), and the numerical simulation result is depicted in Fig. 4 with classification interval of 20 m. Both Fig. 4(a) and Fig. 4(b) correspond to the result of the random forest-based frequency domain classifier, and lower part of Fig. 4(c) shows ISO-B level bound and output of the detailed level decision procedure. On the 400 m sample road, it can be seen from Fig. 4(c) that the overall accuracy of the proposed method is 90%, with 18 out of 20 been accurately estimated. Two error points appear at 200 m and 340 m in Fig. 4(a). Fig. 4(b) reveals that at 200 m, the calculated results at center spatial frequencies of 0.125, 0.25, and 2 cycles/m are ‘Average’ class, and results at 0.0625, 0.5, and 1 cycles/m are ‘Good’ class. In circumstances that both ‘Average’ and ‘Good’ classes have the same number of center spatial frequen-

**Table 3**  
Algorithm 1: Detailed level decision procedure.

---

```

If  $\hat{\Omega}$  is good, then
  If  $|\hat{W}| \geq 2.8$ , then
    SR road condition detected
  Else if  $2.3 \leq |\hat{W}| < 2.8$ , then
    SH road condition detected
  Else if  $|\hat{W}| \leq 2.3$ , then
    ISO-B road condition detected
Else if  $\hat{\Omega}$  is average, then
  HG road condition detected
Else if  $\hat{\Omega}$  is bad, then
  If  $|\hat{W}| \geq 1.8$ , then
    ISO-E road condition detected
  Else if  $|\hat{W}| \leq 1.8$ , then
    PA road condition detected
Else
  Unknown road condition detected
End
 $\hat{\Theta}$  equal to the detected road condition.

```

---

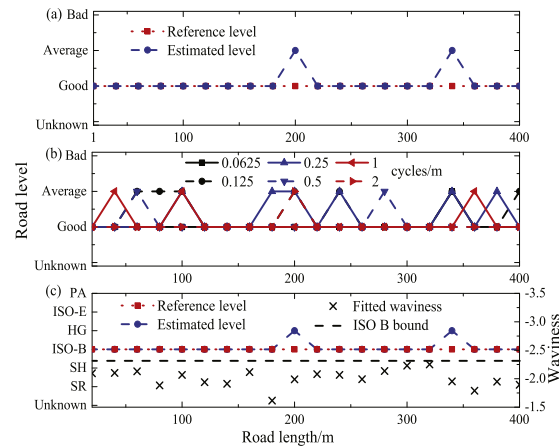


Fig. 4. Classification result: (a) Estimated class, (b) Estimated class at center frequencies, (c) Estimated road level.

cies points, the RF classifier attribute this segment to 'Average' class, and a similar result can be observed at 340 m. Nevertheless, for the estimation at 100 m, although both 'Average' and 'Good' classes have the same number of center spatial frequencies points, the RF classifier classifies this segment to 'Good' class. One solution to this problem is changing the input number of RF classifier to be an odd integer, which can be done in the following ways (1) add one or more center spatial points as the input in the training stage, (2) remove one center spatial point. Both fitted waviness and estimated road level are further illustrated in Fig. 4(c). Fig. 4(c) shows that all of the fitted waviness are larger than  $-2.3$  with a mean value of  $-2.06$ , which means the linear fitting result is accurate enough for the depiction of road input frequency structure. By combining both fitted waviness and result in Fig. 4(a), the overall road level classification result is derived according to the procedure given in Table 3. According to the classification result, the proposed road classification algorithm can accurately estimate road level for the given constant velocity condition, and the results for varying speed scenario will be discussed in the next section.

### 3.3. Simulation results

This part presents numerical simulation results for different driving scenarios. Results of different classification interval, varying velocity, the presence of system uncertainties, and measurement in noisy environments are subsequently discussed. Note that as road profile is randomly generated, the following procedure is taken for all four simulation cases to reduce the influence caused by statistical errors.

- Step 1:** Generate 5000 m length road profile for each of six representative road level;
- Step 2:** Calculate the equivalent road profile  $x_r(t)$  according to generated road profile and vehicle velocity;
- Step 3:** Use bootstrapping to randomly select segments for excitation level estimation, segment length is selected as 50 with re-sampling of 5 times;
- Step 4:** Perform SIRCS and obtain the estimation accuracy by calculating the mean value of the 5 times re-sampling.

#### 3.3.1. Case 1: Influence of classification interval

Selection of classification interval is of great importance for classification accuracy [15]. This paper investigates classification intervals of 10 m, 20 m, 30 m, 40 m and 50 m for all six representative levels, and both estimated waviness  $\hat{W}$  along with classification accuracy (A) are tabulated in Table 4.

**Table 4**  
Accuracy for different classification interval.

Classification interval (m)	Road type (A: classification accuracy)											
	SR		SH		ISO-B		HG		ISO-E		PA	
	$\hat{W}$	A	$\hat{W}$	A	$\hat{W}$	A	$\hat{W}$	A	$\hat{W}$	A	$\hat{W}$	A
10	2.988	74.4%	2.646	54%	1.998	82.8%	2.108	100%	1.958	91.2%	1.558	68.4%
20	3.028	90.4%	2.698	68.8%	2.052	88.4%	2.174	100%	2.08	91.2%	1.628	80%
30	3.056	91.6%	2.726	68.8%	2.046	94.8%	2.164	100%	2.052	95.6%	1.604	80.4%
40	3.076	99.2%	2.708	76.4%	2.056	94.4%	2.192	100%	2.064	96.8%	1.634	81.2%
50	3.074	99.2%	2.712	77.2%	2.074	96.4%	2.158	100%	2.036	96.8%	1.63	84.8%
Definition	3		2.6		2		2.1		2		1.6	



For the estimated waviness, it can be concluded from Table 4 that the estimation error of the waviness in all cases are less than 10% and the influence of classification interval on the estimated waviness is not apparent. All six road levels can output accurate waviness estimation even with the shortest classification interval of 10 m. There is no evidence that a larger classification interval can result in a more accurate waviness estimation. As for the overall classification accuracy, Table 4 shows that increased interval will improve the overall accuracy for road levels, while increment from 10 m to 20 m is much higher than that of longer interval. Generally, a larger classification time means each segment contains more abundant information, which can improve the performance of the statistics characteristics based classifier. Nevertheless, a larger classification time will result in slower reaction to the road variation. Thus a trade-off between classification interval and accuracy exist [15]. In this paper, the classification interval of 20 m is selected for the following simulation discussion and experimental validation.

To further investigate the distribution of the estimated waviness, the Lilliefors test based on the Kolmogorov–Smirnov test is performed for all classification results [39]. The normal probability plot, which was proposed by Chambers [40], is formed by plotting the sorted data vs. an approximation to the means or medians of the corresponding order statistics. If the resulting image looks close to a straight line, then the data are approximately normally distributed. One time run of level ISO-B is performed and shown in Fig. 5 to visualize the distribution.

Fig. 5 shows that the fitted waviness values form an approximately straight line, which indicates that the normal distribution is a good model for the data set [40]. Lilliefors test results for all cases shown in Table 4 further indicates that more than 85% runs accept the null hypothesis at significance level of 5%, and a conclusion that the fitted waviness follows a normal distribution can thus be drawn, which means the proposed algorithm can accurately estimate road PSD structure.

### 3.3.2. Case 2: Classification for velocity-varying scenarios

Simulation result for the varying-velocity case is discussed in the following to illustrate SIRCS performance in the real-world driving scenario. Six representative road levels form a 6000 m road profile with each length of 1000 m. The velocity map is composed of two standard driving cycles, i.e., the EPA inspection and maintenance (IM240) and the highway fuel economy driving schedule (HWFET) [41]. Fig. 6(a) shows the velocity map and sequence of road levels.

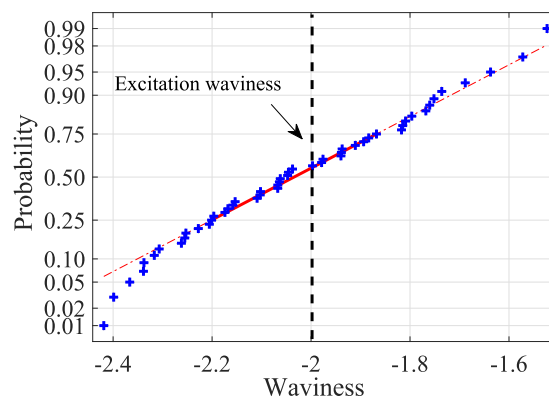


Fig. 5. Lilliefors test result for ISO-B.

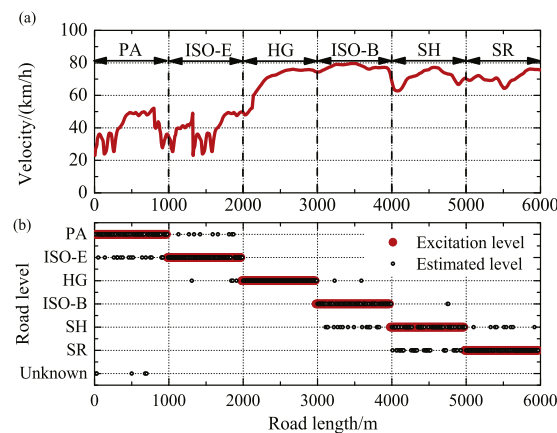


Fig. 6. Classification result for varying velocities.



**Table 5**

Accuracy for varying vehicle velocity.

Road level		Classified level							Accuracy
		PA	ISO-E	HG	ISO-B	SH	SR	Unknown	
True level	PA	76	18	–	–	–	–	5	76.7%
	ISO-E	8	88	4	–	–	–	–	88%
	HG	–	–	100	–	–	–	–	100%
	ISO-B	–	–	2	81	17	–	–	81%
	SH	–	–	–	6	64	30	–	64%
	SR	–	–	–	–	9	91	–	91%

**Table 6**

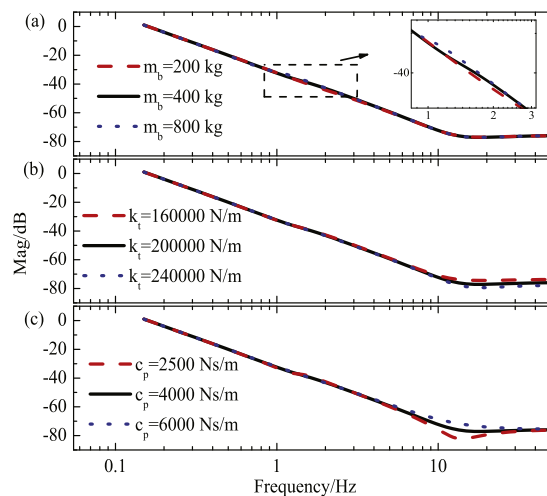
Accuracy of system with uncertainties.

Parameters		Accuracy
$m_b$	Nominal	88.4%
	340	84.8%
	480	85.6%
$c_p$	2500	87.2%
	6000	77.2%
$k_t$	160,000	77.6%
	240,000	86.8%

Generally, the vehicle intends to drive slower in the poor road and faster in good profile conditions. As the classification is selected as 20 m in case 1, this paper adopts a 20 m moving window with 10 m from previous frame, i.e., 50% overlap. Such overlapping results in a void output at the 10 m point, and results in 99 points output for PA. With the proposed SIRCS introduced in Section 3.2, the classification result is shown in Fig. 6(b) and Table 5. Both Fig. 6(b) and Table 5 indicate that the proposed SIRCS can successfully classify the unknown road input with an accuracy of more than 75% except for the SH. Table 5 indicates there are 5 unknown points occurred during the PA excitation, which means 5 samples are mistakenly classified to be “Very poor” class by the frequency domain classifier. Further, it can be seen that 36 points of SH are mislabeled to be SR and ISO-B, and the reason is the fitted waviness is bounded on both sides in Table 3. To sum up, the difference between varying velocity scenario and consistent velocity result given in Table 4 is not apparent, which indicates that the proposed SIRCS is independent of changes in vehicle velocity.

### 3.3.3. Case 3: Classification with the presence of parameters uncertainties

The existence of parameters uncertainties will result in a variation of suspension system responses [42]. For parameters of quarter vehicle model shown in Table 6, the sprung mass  $m_b$  varies due to load variation, the suspension damper coefficient  $c_p$  changes because of long time operation and application of controllable damper system [43], and the tire stiffness alters owing to tire pressure fluctuation [44]. Based on the transfer function Eq. (2), Fig. 7 depicts the influence of varying  $x_b$ ,  $k_t$  and  $c_p$  on unsprung mass acceleration in the frequency domain.

**Fig. 7.** Transfer function for varying system parameters: (a) sprung mass, (b) tire stiffness, (c) damper coefficient.

Generally, the influence of parameters uncertainties on sprung mass acceleration is inconspicuous. Fig. 7(a) shows that sprung mass has little effect on the transfer function even around the sprung mass resonant frequency of 1 Hz. Compared to the sprung mass, variation of tire stiffness and damper coefficient cause relatively large fluctuation in the high frequency range especially around unsprung mass resonant frequency, and the largest change is about 6 dB for  $c_p = 6000$  Ns/m compared to  $c_p = 4000$  Ns/m.

To further illustrate the influence of system parameters uncertainties on classification accuracy, a variation of 20% on sprung mass, 30% on damper coefficient and 15% on tire stiffness are individually investigated on road level ISO-B. According to the results shown in Table 7, a decrease of damper coefficient, an increase of tire stiffness and both cases for sprung mass do not dramatically influence the classification accuracy. As for increased  $c_p$  and decreased  $k_t$ , the mean accuracy deteriorates from more than 86%–77%. Both Fig. 7(b) and (c) show that these two scenarios lead to an increment of the transfer function in the high frequency range, and the proposed SIRCS is more sensitive to such variations of  $c_p$  and  $k_t$ .

### 3.3.4. Case 4: Classification with measurement noise

The above discussions and conclusions are derived based on ideal measurement assumption, but the measurement noise is typically unavoidable in a real-world application. In this case, the influence of unsprung mass acceleration measurement noise is firstly discussed, a method to improve classification accuracy for large noise scenario is subsequently proposed. The noise level is defined by the signal-to-noise ratio (SNR) by the following equation:

$$SNR = \frac{P_{signal}}{P_{noise}} = \frac{\sigma_{signal}^2}{\sigma_{noise}^2} \quad (6)$$

where  $P_{signal}$  and  $\sigma_{signal}^2$  are the signal power and variance of unsprung mass acceleration. Fig. 8 shows the ISO-B level PSD of  $x_r(t)$  corrupted by white noise with SNR equals to 10, 20 and 40. Considering the randomness of noise, The red lines of each case are results of 20 times run with different white noise seeds. It can be seen from Fig. 8 that increment of measurement noise results in an overestimation of road PSD especially in the low-frequency range, and influence on the high-frequency range can be neglected even for the high noise variance of SNR = 10. For spatial frequency of 0.0625 cycles/m, the estimated road PSD reaches the next ISO level, which will make the classifier mislabeling this point to be “Average” class. In this case, the lower spatial frequency can be considered to be removed from classifier input when the adopted sensors are sensitive to the measurement noise. To further illustrate this, classification results for the worst case, i.e. SNR = 10 are tabulated in Table 7. The term ‘combination’ stands for the input set of the frequency domain based classifier:

- All six center spatial frequencies.
- Five center spatial frequencies except 0.0625 cycles/m.

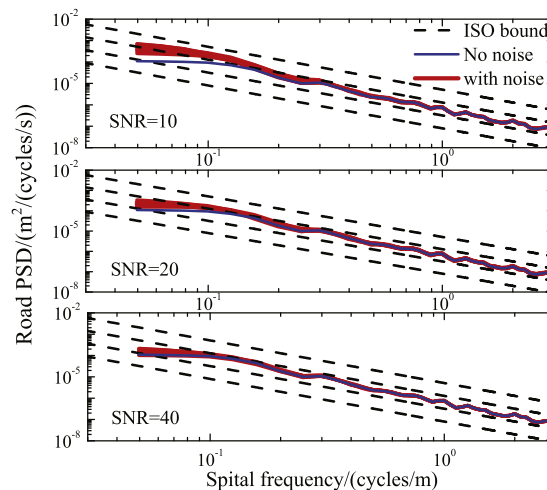


Fig. 8. Influence of measurement noise on the transfer function.

Table 7

Accuracy for different measurement noise.

Accuracy	SR	SH	ISO-B	HG	ISO-E	PA
Combination 1	68.4%	59.4%	80.8%	99.6%	80.6%	68.4%
Combination 2	71.2%	61.6%	82%	99.6%	82%	72.2%
Combination 3	70.4%	62.6%	81.6%	99.4%	84%	72.5%

- Four center spatial frequencies apart from 0.0625 and 0.125 cycles/m.

Table 7 shows that large measurement noises will degrade SIRCS performance. Considering the overestimation caused by the measurement noise, combination 1 performs worse than both combinations 2 and 3, while combinations 2 and 3 perform the same level. This means the estimated road PSD in the lower center spatial frequencies are much sensitive to measurement noise. The operator can thus remove the first spatial frequency, i.e., 0.0625 cycles/m to improve classification accuracy when grinding measurement noise is unavoidable.

#### 4. Experimental validation

In this section, a field test was performed to validate the SIRCS. The experiments were performed in the test track of the region of Waterloo, ON, Canada. Fig. 9 shows the image of the test field, and two different types of road, i.e. pavement and gravel. A Cadillac CTS was adopted as the experimental car, with accelerometer Kistler 8305 and tachometer installed on the hub of the front left wheel. The system measurements and signal processing procedures are shown in Fig. 10. The Micro-Autobox was configured to receive vehicle wheel speed and unsprung mass acceleration on the CAN network, and the proposed algorithm attributed the road input to the level with the road classification.

To evaluate the performance of the proposed method, three velocity values of 20, 50, and 80 km/h and passenger numbers of one and four were adopted. The experimental conditions are tabulated in Table 8. The sample rate was set at 1000 Hz, and the sampled signal firstly passed through a bandpass filter with cut-off frequencies of 0.3 Hz and 100 Hz. Fig. 11 further shows the sampled data for condition No. 7. With sampled unsprung mass acceleration in Fig. 11(b), the equivalent road profile  $x_r(t)$  is first calculated according to Eq. (2) in Fig. 11(c) (in the time domain). Vehicle velocity was then used to generate

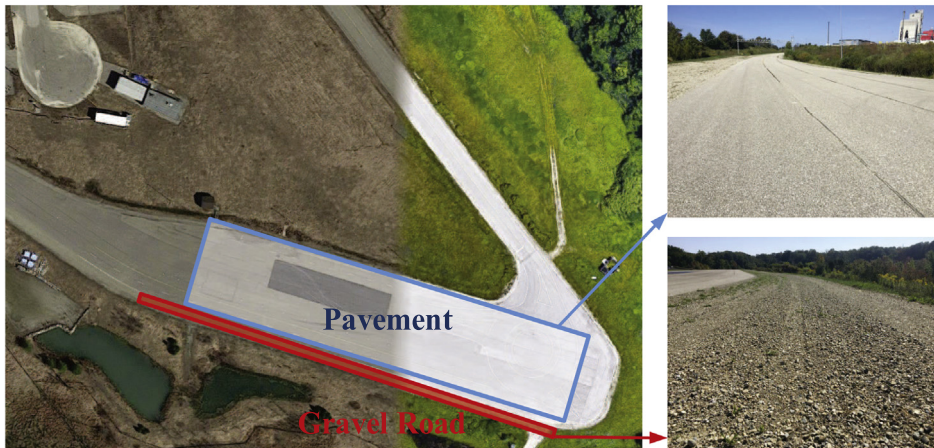


Fig. 9. Experiment field with pavement and gravel road (Image courtesy of Google Map).

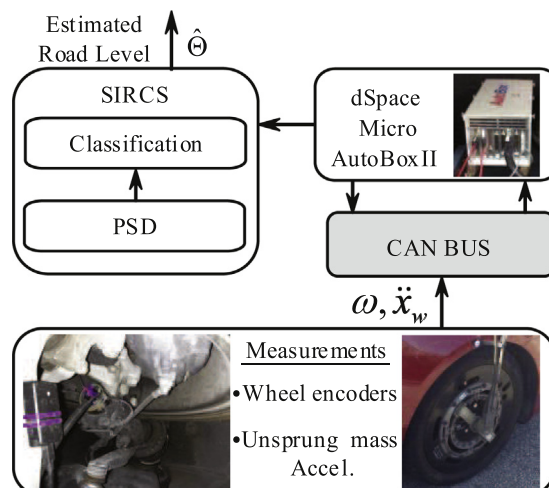
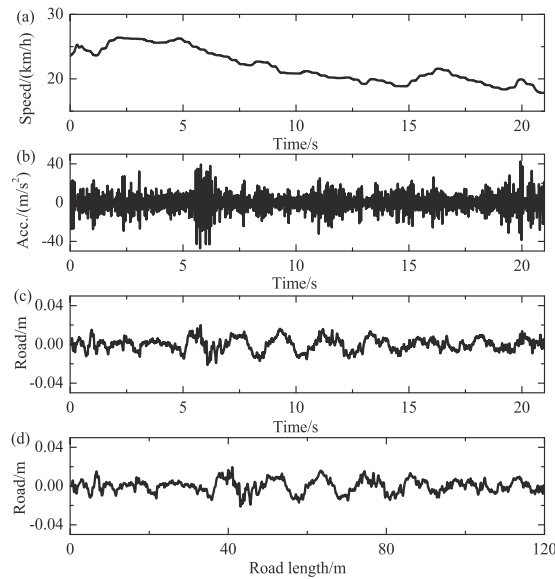


Fig. 10. Measurement and classification with the experiment vehicle.

**Table 8**  
Experiment list.

No.	Road type	Velocity (km/h)	Passenger number	Duration (s)
1	Pavement	20	4	20
2	Pavement	50	4	6
3	Pavement	80	4	21
4	Pavement	20	1	17
5	Pavement	50	1	8
6	Pavement	80	1	5
7	Gravel	20	4	21
8	Gravel	50	4	12
9	Gravel	80	4	4



**Fig. 11.** Experiment results for test No. 7, (a) Velocity, (b) Unsprung mass acceleration, (c) Equivalent road profile in the time domain, (d) Estimated road in the spatial domain.

the estimated road profile in the spatial domain from the equivalent road profile as in Fig. 11(d). According to Fig. 11(d), such transformation did not change the estimated road amplitude, and influence of the varying velocities on  $x_r(t)$  is removed. The classification results are finally derived as per the two-step classifier discussed in Section 3. Note that since road level SR represents the ideal runway and typically located inside the airport, it is not considered during experimental validation.

As there is no prior information for the two types road profile, PSD of the estimated road profile in the spatial domain for all 9 tests are given in Fig. 12. In Fig. 12, all tests conducted on the pavement are shown in green, and another three tests in

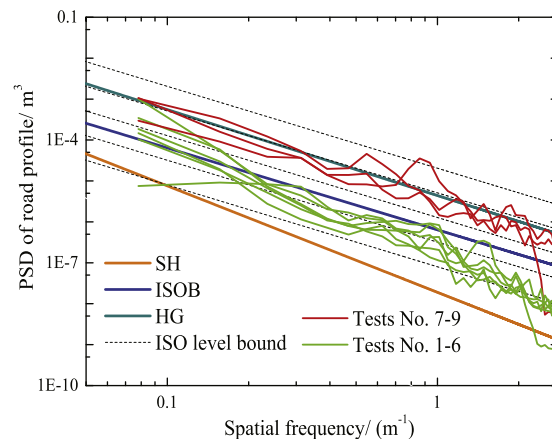


**Fig. 12.** Estimated road PSD of experiments.

**Table 9**

Experiment classification result.

Combination	SH	ISO-B	HG	ISO-E	Excitation level	Accuracy
No. 1 (Test 1–3)	53	11	1	–	SH	81.5%
No. 2 (Test 4–6)	19	5	1	–	SH	76.1%
No. 3 (Test 7–9)	–	3	30	–	HG	90.9%

red stand for the gravel road condition. It is obvious that the gravel road fit the standard HG PSD well with waviness of about 2. As for the pavement, since most components of the estimated road in frequency domain locate between SH and ISO-B, it is acceptable to attribute the pavement into either of the two levels from the viewpoint of excitation energy. From the perspective of the waviness, the fitted waviness of tests No. 1–6 are  $-2.69$ ,  $-2.54$ ,  $-2.68$ ,  $-2.71$ ,  $-2.49$ , and  $-2.68$ , respectively. It should be mentioned that the mean value of these 6 runs waviness equals to  $-2.63$  that is close to  $-2.6$  of SH. To sum up, SH is adopted as the excitation level for runs No. 1–6.

To reduce the influence of measurement noise, the last five center spatial frequencies, i.e., 0.125, 0.25, 0.5, 1, and 2 cycles/m, are taken as the input to the RF classifier in this section. The proposed SIRCS is finally used to classify road excitation. The classification results are tabulated in Table 9. The 9 tests are further divided into 3 groups, representing the nominal condition in the SH, the varying sprung mass condition in the SH, and the nominal condition in the HG. By and large, classification accuracy in Table 9 indicates that the proposed two-step can accurately classify road input into accurate representative road levels. For Combination No. 3, 30 points are attributed to correct excitation level, with only 3 points being classified to ISO-B, which means the proposed algorithm can precisely estimate the road level when the excitation has similar excitation energy and PSD structure with one representative road level. For Combination No. 1, 12 sample segments are mislabeled, and the overall accuracy is 81.5%. It can be seen from these errors that 11 out of 12 points are attributed to ISO-B. The reason can be interpreted as both ISO-B and SH are 'Good' road class, and the detailed level is determined based on only road waviness, so the PSD fluctuations caused by transient events result in the errors. As for Combination No. 2, which corresponding to the varying sprung mass case, the estimation accuracy is 76.1%. Since the accuracy difference between Combination No.2 and No. 1 is not apparent; the conclusion that the proposed SIRCS can robustly classify road profile without any pre-training process can be drawn.

## 5. Conclusion

This paper presents a road classification framework called SIRCS that can accurately classify road levels by only unsprung mass acceleration data. The proposed strategy depends only on the transfer function from unsprung mass acceleration to road excitations. The influence of vehicle speed is removed in the online phase. Numerical simulations for different scenarios indicated the proposed method is robust to system parameters uncertainties and measurement noises. In addition, the field test results further validate this strategy with an accuracy of more than 75%. According to both numerical and experimental studies, the following conclusions are drawn:

- Unsprung mass acceleration is quite suitable for road estimation as suspension parameters have little impact on the road classification.
- The choice of representative road levels is critical for the proposed road classification algorithm. Road conditions with similar excitation energy and waviness will dramatically influence classifier's performance.
- Large measurement noises result in overestimation of the fitted waviness. Thus prior SNR information would be beneficial.

Further research will focus on the following aspects:

- Road classification with large amount of sampled data and route planning based on road condition map.
- Influence of transient events on vehicle vertical response and road anomaly detection algorithm.

## Acknowledgments

This work was supported of Beijing Natural Science Foundation (Grant No. 3184058), National Natural Science Foundation of China (Grant No. U1564210), and China Postdoctoral Science Foundation (Grant No. 2016M600934, Grant No. BX201600017).

## References

- [1] G. Xue, H. Zhu, Z. Hu, J. Yu, Y. Zhu, Y. Luo, Pothole in the dark: perceiving pothole profiles with participatory urban vehicles, *IEEE Trans. Mob. Comput.* 16 (5) (2017) 1408–1419.
- [2] Z.F. Wang, M.M. Dong, L. Gu, J.J. Rath, Y.C. Qin, B. Bai, Influence of road excitation and steering wheel input on vehicle system dynamic responses, *Appl. Sci.* 7 (6) (2017) 570.

- [3] TRIP, America's roughest rides and strategies to make our roads smoother, The Road Information Program (TRIP), Washington, DC.
- [4] DGIP, EU road surfaces: economic and safety impact of the lack of regular road maintenance, European Parliament's Committee on Transport and Tourism.
- [5] X. Tang, W. Yang, X. Hu, D. Zhang, A novel simplified model for torsional vibration analysis of a series-parallel hybrid electric vehicle, *Mech. Syst. Sig. Process.* 85 (2017) 329–338.
- [6] Z. Li, I.V. Kolmanovskiy, E.M. Atkins, J. Lu, D.P. Filev, Y. Bai, Road disturbance estimation and cloud-aided comfort-based route planning, *IEEE Trans. Cybern.* (2017).
- [7] Y. Huang, A. Khajepour, T. Zhu, H. Ding, A supervisory energy-saving controller for a novel anti-idling system of service vehicles, *IEEE/ASME Trans. Mechatron.* 22 (2) (2017) 1037–1046.
- [8] T. Liu, X. Hu, S.E. Li, D. Cao, Reinforcement learning optimized look-ahead energy management of a parallel hybrid electric vehicle, *IEEE/ASME Trans. Mechatron.* 22 (4) (2017) 1497–1507.
- [9] C. Hu, R. Wang, F. Yan, Y. Huang, H. Wang, C. Wei, Differential steering based yaw stabilization using ismc for independently actuated electric vehicles, *IEEE Trans. Intell. Transp. Syst.* 19 (2) (2018) 627–638.
- [10] Y. Qin, C. Wei, X. Tang, N. Zhang, M. Dong, C. Hu, A novel nonlinear road profile classification approach for controllable suspension system: Simulation and experimental validation, *Mech. Syst. Sig. Process.* (2018), <https://doi.org/10.1016/j.ymssp.2018.07.015>.
- [11] H. Iminé, Y. Delanne, N. M'sirdi, Road profile input estimation in vehicle dynamics simulation, *Vehicle Syst. Dyn.* 44 (4) (2006) 285–303.
- [12] Y. Qin, M. Dong, F. Zhao, R. Langari, L. Gu, Road profile classification for vehicle semi-active suspension system based on adaptive neuro-fuzzy inference system, 54th IEEE Annual Conference on Decision and Control (CDC), IEEE, 2015, pp. 1533–1538.
- [13] Z. Wang, M. Dong, Y. Qin, Y. Du, F. Zhao, L. Gu, Suspension system state estimation using adaptive kalman filtering based on road classification, *Vehicle Syst. Dyn.* 55 (3) (2017) 371–398.
- [14] C.C. Ward, K. Iagnemma, Speed-independent vibration-based terrain classification for passenger vehicles, *Vehicle Syst. Dyn.* 47 (9) (2009) 1095–1113.
- [15] Y. Qin, R. Langari, Z. Wang, C. Xiang, M. Dong, Road excitation classification for semi-active suspension system with deep neural networks, *J. Intell. Fuzzy Syst.* 33 (3) (2017) 1907–1918.
- [16] Y. Qin, C. Xiang, Z. Wang, M. Dong, Road excitation classification for semi-active suspension system based on system response, *J. Vib. Control* 24 (13) (2018) 2732–2748, <https://doi.org/10.1177/1077546317693432>.
- [17] Z. Li, U.V. Kalabić, I.V. Kolmanovskiy, E.M. Atkins, J. Lu, D.P. Filev, Simultaneous road profile estimation and anomaly detection with an input observer and a jump diffusion process estimator, 2016 American Control Conference (ACC), IEEE, 2016, pp. 1693–1698.
- [18] H. Zhang, J. Wang, Adaptive sliding-mode observer design for a selective catalytic reduction system of ground-vehicle diesel engines, *IEEE/ASME Trans. Mechatron.* 21 (4) (2016) 2027–2038.
- [19] H. Zhang, G. Zhang, J. Wang,  $H_\infty$  observer design for LPV systems with uncertain measurements on scheduling variables: application to an electric ground vehicle, *IEEE/ASME Trans. Mechatron.* 21 (3) (2016) 1659–1670.
- [20] F. Zhao, S.S. Ge, F. Tu, Y. Qin, M. Dong, Adaptive neural network control for active suspension system with actuator saturation, *IET Control Theor. Appl.* 10 (14) (2016) 1696–1705.
- [21] J. Rath, K.C. Veluvolu, M. Defoort, Simultaneous estimation of road profile and tire road friction for automotive vehicle, *IEEE Trans. Veh. Technol.* 64 (10) (2015) 4461–4471.
- [22] Y. Qin, R. Langari, Z. Wang, C. Xiang, M. Dong, Road profile estimation for semi-active suspension using an adaptive kalman filter and an adaptive super-twisting observer, 2017 American Control Conference (ACC), IEEE, 2017, pp. 973–978.
- [23] W. Fauriat, C. Mattrand, N. Gayton, A. Beakou, T. Cembrzynski, Estimation of road profile variability from measured vehicle responses, *Vehicle Syst. Dyn.* 54 (5) (2016) 585–605.
- [24] A. Gonzalez, E.J. O'Brien, K. Cashell, The use of vehicle acceleration measurements to estimate road roughness, *Vehicle Syst. Dyn.* 46 (6) (2008) 483–499.
- [25] S. Wang, S. Kodagoda, L. Shi, H. Wang, Road-terrain classification for land vehicles: employing an acceleration-based approach, *IEEE Veh. Technol. Mag.* 12 (3) (2017) 34–41.
- [26] H. Pacejka, *Tire and Vehicle Dynamics*, Elsevier, 2005.
- [27] M. Mitschke, H. Wallentowitz, *Vehicle Dynamics*, Qinghua University Press, 2009.
- [28] H. Li, J. Yu, C. Hilton, H. Liu, Adaptive sliding-mode control for nonlinear active suspension vehicle systems using t-s fuzzy approach, *IEEE Trans. Industr. Electron.* 60 (8) (2013) 3328–3338.
- [29] O. Kropáč, P. Múčka, Effects of longitudinal road waviness on vehicle vibration response, *Vehicle Syst. Dyn.* 47 (2) (2009) 135–153.
- [30] J.Y. Wong, *Theory of Ground Vehicles*, John Wiley & Sons, 2008.
- [31] ISO, *Mechanical vibration-road surface profiles-reporting of measured data* (1995).
- [32] Y. Qin, C. He, X. Shao, H. Du, C. Xiang, M. Dong, Vibration mitigation for in-wheel switched reluctance motor driven electric vehicle with dynamic vibration absorbing structures, *J. Sound Vib.* 419 (2018) 249–267.
- [33] E. Hashemi, M. Pirani, A. Khajepour, A. Kasaiezadeh, S.-K. Chen, B. Litkouhi, Corner-based estimation of tire forces and vehicle velocities robust to road conditions, *Control Eng. Pract.* 61 (2017) 28–40.
- [34] E. Hashemi, M. Pirani, A. Khajepour, B. Fidan, A. Kasaiezadeh, S.-K. Chen, Opinion dynamics-based vehicle velocity estimation and diagnosis, *IEEE Trans. Intell. Trans. Syst.* (2017).
- [35] D. Selmanaj, M. Corno, G. Panzani, S.M. Savaresi, Vehicle sideslip estimation: a kinematic based approach, *Control Eng. Pract.* 67 (2017) 1–12.
- [36] E. Hashemi, S. Khosravani, A. Khajepour, A. Kasaiezadeh, S.-K. Chen, B. Litkouhi, Longitudinal vehicle state estimation using nonlinear and parameter-varying observers, *Mechatronics* 43 (2017) 28–39.
- [37] A. Katriniok, D. Abel, Adaptive ekf-based vehicle state estimation with online assessment of local observability, *IEEE Trans. Control Syst. Technol.* 24 (4) (2016) 1368–1381.
- [38] L. Breiman, Random forests, *Mach. Learn.* 45 (1) (2001) 5–32.
- [39] W.J. Conover, W.J. Conover, *Practical nonparametric statistics*.
- [40] J.M. Chambers, W.S. Cleveland, B. Kleiner, P.A. Tukey, et al, *Graphical Methods for Data Analysis*, Vol. 5, Wadsworth Belmont, CA, 1983.
- [41] United States Environmental Protection Agency, Dynamometer drive schedules, <https://www.epa.gov/vehicle-and-fuel-emissions-testing/dynamometer-drive-schedules>.
- [42] W. Sun, H. Pan, Y. Zhang, H. Gao, Multi-objective control for uncertain nonlinear active suspension systems, *Mechatronics* 24 (4) (2014) 318–327.
- [43] Y. Qin, F. Zhao, Z. Wang, L. Gu, M. Dong, Comprehensive analysis for influence of controllable damper time delay on semi-active suspension control strategies, *J. Vib. Acoust.* 139 (3) (2017) 031006.
- [44] I. Besselink, A. Schmeitz, H. Pacejka, An improved magic formula/swift tyre model that can handle inflation pressure changes, *Vehicle Syst. Dyn.* 48 (S1) (2010) 337–352.